ARTICLES
https://doi.org/10.1038/s41928-022-00823-w

nature electronics

Check for updates

OPEN

An integrated magneto-optic modulator for cryogenic applications

Paolo Pintus[1,2]✉, Leonardo Ranzani[3], Sergio Pinna[1], Duanni Huang[1,4], Martin V. Gustafsson[3], Fotini Karinou[5], Giovanni Andrea Casula[6], Yuya Shoji[7], Yota Takamura[7], Tetsuya Mizumoto[7], Mohammad Soltani[3] and John E. Bowers[1]

Superconducting circuits can operate at higher energy efficiencies than their room-temperature counterparts and have the potential to enable large-scale control and readout of quantum computers. However, the required interface with room-temperature electronics creates difficulties in scaling up such cryogenic systems. One option is to use optical fibres as a medium in conjunction with fast optical modulators that can be efficiently driven by electrical signals at low temperatures. However, as superconducting circuits are current operated with low impedances, they interface poorly with conventional electro-optical modulators. Here we report an integrated current-driven modulator that is based on the magneto-optic effect and can operate at temperatures as low as 4 K. The device combines a magneto-optic garnet crystal with a silicon waveguide resonator and integrates an electromagnet to modulate the refractive index of the garnet. The modulator offers data rates of up to 2 Gbps with an energy consumption below 4 pJ per bit of transferred information, which could be reduced to less than 50 fJ per bit by replacing dissipative electrodes with superconductors and optimizing the geometric parameters.

In classical and quantum cryogenic computing systems, there is a need to transfer massive amounts of information from cryogenic circuitry to room temperature, as well as minimizing the hardware complexity and heat load. This becomes particularly challenging as systems are scaled up given the limited physical space and cooling power available in cryogenic systems. The issue can be addressed with photonic integrated circuits operating at low temperatures and the use of optical fibres to connect different temperature stages, thus enabling scalable, low-cost and power-efficient optical interconnections for large data transfer rates[1–3].

Silicon photonics is arguably the most promising technology platform for the development of cryogenic photonic integrated circuit components, due to its high scalability, excellent optical performance and compatibility with complementary metal–oxide–semiconductor and superconducting electronics fabrication[4]. However, low temperatures (for example, below 4 K) create important limitations for conventional silicon modulators and switches. Thermo-optic (TO) switches become non-functional due to a considerable drop in TO coefficient[5], and modulators based on plasma dispersion suffer from free-carrier freeze-out, which reduces their efficiency[6]. The carrier freeze-out effect can be compensated by augmenting the doping concentration, but only at the cost of increased optical absorption[7].

To date, only electro-optic modulators have been shown to work at low temperatures[2,7–11], and the use of magneto-optical (MO) effects in integrated optics has been limited to optical isolators and circulators[12,13], although there are a few theoretical proposals existing for MO modulation[14–16]. This is largely due to the difficulties in manufacturing integrated MO devices, the challenges involved in applying fast time-variant magnetic fields and the generally slower response of the MO effect compared with the electro-optic effect.

In this Article, we report a high-speed MO modulator operating at temperatures as low as 4 K. The device is created by combining an MO garnet crystal with a silicon waveguide resonator and integrating an electromagnet to modulate the refractive index of the garnet. The device is particularly efficient at cryogenic temperatures, where the MO effect becomes stronger[17] and the power consumption in the electromagnet decreases drastically compared with room temperature due to the reduced ohmic loss. We show that the modulator can offer data rates of up to 2 Gbps with an energy consumption as low as 4 pJ per bit of transferred information, which could be reduced to below 50 fJ per bit if the electrodes are replaced by superconductors and the fabrication process is further optimized. Our current-driven MO modulator can be of use in the development of power-efficient data links for the next generation of superconducting supercomputers and interface circuits for quantum computers[18–23].

Integrated MO modulator

Our modulator is based on an all-pass silicon microring resonator with a cerium-substituted yttrium iron garnet (Ce:YIG) bonded on top (Fig. 1a). The light that circulates in the microring resonator interacts evanescently with the garnet, and is affected by its MO properties. A gold coil, aligned with the silicon microring, serves as an integrated electromagnet and is used to control the MO properties of Ce:YIG, whereas a silicon waveguide is used to couple light in and out of the resonator.

The main idea of our work is to exploit the refractive-index variation induced by an applied magnetic field to control the resonant wavelength of the microring and hence modulate the light passing through the waveguide. When an electrical current flows through the coil, Ce:YIG is magnetized by a in-plane transverse-magnetic field (Fig. 1b), changing the effective refractive index of the optical

[1]Department of Electrical and Computer Engineering, University of California Santa Barbara, Santa Barbara, CA, USA. [2]Department of Physics, University of Cagliari, Monserrato, Italy. [3]Raytheon BBN Technologies, Cambridge, MA, USA. [4]Intel Corporation, Santa Clara, CA, USA. [5]Microsoft Research Ltd., Cambridge, UK. [6]Department of Electrical and Electronic Engineering, University of Cagliari, Via Castelfidardo, Cagliari, Italy. [7]Department of Electrical and Electronic Engineering, Tokyo Institute of Technology, Meguro-ku, Japan. ✉e-mail: ppintus@ece.ucsb.edu

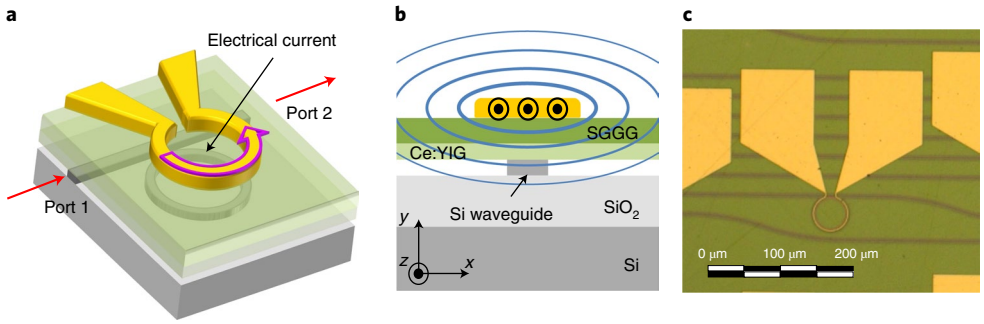

Fig. 1 | Integrated MO modulator. a, Perspective view of the device (not to scale). The top gold coil is used to apply a radial magnetic field to Ce:YIG underneath, making it non-reciprocal. The silicon microring and silicon waveguide, in the all-pass filter configuration, are visible through the transparent top cladding. **b**, Cross-section of the microring and electromagnet (not to scale) where the direction of the electrical current and magnetic field are highlighted. **c**, Optical micrograph of the fabricated sample (top view).

mode[24] (Supplementary Section 1). For the microring, a variation in the effective index, Δn_{eff}, causes a proportional shift in the optical spectrum of the resonator:

$$\Delta\lambda_{\mathrm{MO}} = \lambda\frac{\Delta n_{\mathrm{eff}}}{n_{\mathrm{g}}}, \quad (1)$$

where λ is the optical wavelength and n_{g} is the group refractive index of the optical mode[25]. If an applied current causes the resonant wavelength of the microring to tune towards the wavelength of the optical input signal, light is dissipated in the microring and transmission through the waveguide decreases. When the direction of the current is reversed, the microring resonance tunes away from the wavelength of the incoming light, which can then propagate through the waveguide with reduced attenuation. Based on this concept, we designed and fabricated the device shown in Fig. 1c.

Equation (1) and Fig. 1a–c are crucial for understanding the operating principle of this device; therefore, we highlight a few important features: (1) reversing the current (that is, flipping the in-plane magnetic field in Ce:YIG) changes the sign of Δn_{eff}; (2) the effective index change differs for the clockwise (CW) and counterclockwise (CCW) propagating modes, having the same amplitude but opposite signs (non-reciprocal effect); (3) the effective index change is the largest when the optical mode is polarized along the y axis (transverse-magnetic polarized mode); (4) the value of the effective index change is proportional to the Faraday rotation constant (Supplementary Section 1), which is expected to increase with decreasing temperature[17,26].

Modelling and fabrication of the MO modulator

The results of the modelling and device design are summarized in Fig. 2. The magnetic-field distribution (Fig. 2a) is obtained after optimizing the cross-section of the gold coil (Fig. 2b) and the optical waveguide (Fig. 2c) to produce the largest shift in resonance wavelength for a given current. For the realization of this first prototype, we chose Ce:YIG as the MO material because it is optically transparent to telecom wavelengths (~1,550 nm) and has one of the largest Faraday rotation constants in this wavelength range at room temperature. The optimized cross-section of the silicon waveguide is 600 nm wide and 220 nm tall, with a 400-nm-thick Ce:YIG layer bonded on top[27]. To avoid bending loss, the diameter of the microring is chosen to be 70 μm. At room temperature, this cross-section guarantees $\Delta\lambda_{\mathrm{MO}} = \pm 300$ pm when the magnetization of the material is saturated in the two directions[27], that is, $\mu_0|H_x| \geq 5$ mT (50 Oe). A layer of 5-μm-thick substituted gadolinium gallium garnet (SGGG) covers Ce:YIG and is a remnant of the substrate onto which Ce:YIG was grown. On top of this layer, directly above the silicon microring, a circular gold electrode with a cross-section of 3.0 μm × 1.5 μm is patterned. This is the electromagnet that transduces the modulation current into a time-variant magnetic field through Ce:YIG.

The current flowing through the electromagnet can be used to redshift or blueshift the resonance of the microring, depending on its direction. At 4 K, the thermal shift of the microring resonance is negligible[5,28]. To perform amplitude modulation, the input laser wavelength is tuned to be at the 3 dB cutoff wavelength of the modulator transfer function when no current is injected in the electromagnet (λ_{tbm}; Fig. 2d). The current in the electromagnet is used to bring the resonance of the microring closer to or further away from the input wavelength. When the current in the electromagnet alternates between −110 and +110 mA, it generates an in-plane magnetic field of ±1.5 mT (±15 Oe) at the interface silicon/Ce:YIG, producing a resonance shift of ±20 pm at 4 K. Despite Ce:YIG showing hysteresis in the magnetization field at low temperatures, the resonance shift remains linear with respect to current due to the coercive field being larger than the magnetic field that is applied here. The slope of the MO response scales as the ratio of the maximum MO response to the coercive field (Supplementary Section 3.4).

The highest extinction ratio (ER) is achieved when the resonance is shifted by half of the full-width at half-maximum (FWHM) (Fig. 2d). In this context, the resonator quality factor Q plays a critical role. A higher quality factor produces a narrower FWHM and higher ER, allowing the same modulation with lower current and hence lower power consumption. On the other hand, an excessively large value of Q results in a long cavity photon lifetime that limits the optical bandwidth, which is given by $\mathrm{BW}_0 = \omega_0/2\pi Q$, where ω_0 is the optical angular frequency[29–31]. In the fabricated device, the optical loss in Ce:YIG limits the intrinsic Q value to 43,000 (Supplementary Section 3.3).

The device performance is optimized by engineering the power coupling ratio K between the microring and waveguide. Figure 2e shows the ER of the modulated signal as a function of the current amplitude for different coupling conditions. When K equals the intrinsic cavity loss per round-trip γ (critical coupling condition), the ER can, in principle, be chosen to be arbitrarily large[27], limited only by fabrication variabilities. For this condition, the optical bandwidth is ~8.5 GHz. Comparing overcoupled ($K > \gamma$) and undercoupled ($K < \gamma$) resonators with the same maximum ER, we note that the undercoupled condition is more favourable for minimizing the driving current and hence the energy consumption, at the cost of a smaller optical bandwidth. Because of these considerations, we choose to operate in the overcoupled regime. With a loaded quality factor of $Q = 16{,}000$, we expect $\mathrm{BW}_0 > 12$ GHz and ER > 10 dB.

A notable feature of this device architecture is the reduction in energy consumption for modulation at low temperatures compared

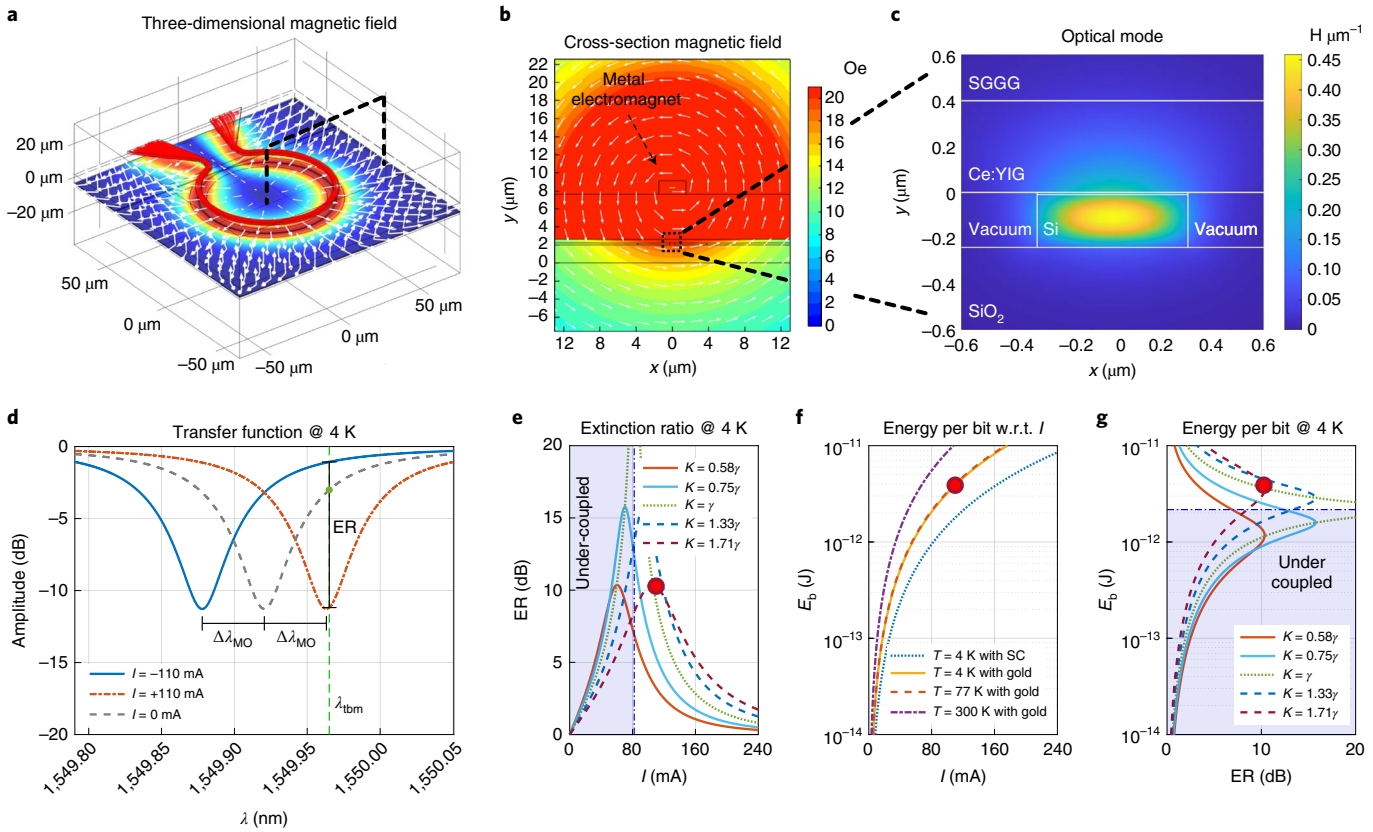

Fig. 2 | Cryogenic MO modulator, design and optimization. a, Magnetic field generated by the electric current in the metal coil (electromagnet). The streamlines of the current are highlighted in red, whereas the intensity of the in-plane radial magnetic field is shown in the Ce:YIG plane. On the same plane, the arrows indicate the direction of the magnetic field. **b**, Magnetic-field distribution in the device cross-section for a current of 110 mA. **c**, Profile of the transverse-magnetic optical mode (the main magnetic-field component) computed assuming a 10-nm-thick silica layer between the silicon and Ce:YIG layers. **d**, Calculated redshifted and blueshifted spectral response of the device when the current is +110 mA (dashed pointed red curve) and −110 mA (solid blue curve), respectively. As a reference, the spectral response when no current is injected is also plotted (dashed grey curve). These curves refer to a microring resonator with a full-width at half-maximum $\Lambda_{FWHM} = 97$ pm, such that the loaded $Q = \lambda/\Lambda_{FWHM}$ equals 16,000. The input laser wavelength is shown (λ_{tbm}, green dashed line) along with the ER and MO shift ($\pm\Delta\lambda_{MO}$). **e**, ER as a function of modulation current for several microring-based modulators with different coupling coefficients (K) to the waveguide. The dot refers to the DUT, where the coupling coefficient ($K = 0.11$) and the round-trip loss ($\gamma = 0.063$) are computed from the measured ER and FWHM of the spectral response. **f**, Modelled energy consumption per bit as a function of the modulation current at different temperatures for a modulation rate of 2 Gbps (the experimental values of gold conductivity at 300, 77 and 4 K are considered). In the case of a superconducting (SC) magnet, the power dissipated in the resistance of the coil vanishes, leaving only the $LI^2/2$ component of dissipation. The dot refers to the DUT. **g**, Energy per bit as a function of ER in the undercoupled, critically coupled and overcoupled conditions. The simulations refer to the case of gold contacts, at a temperature of 4 K, with a modulation rate of 2 Gbps. The dot refers to the DUT.

with room temperature. The average energy-per-bit consumption of the modulator is

$$\overline{E_b} = \frac{RI^2}{r_b} + \frac{LI^2}{2}, \quad (2)$$

where R and L are the effective resistance and inductance of the electromagnet, respectively; I is the amplitude of the modulation current; and r_b is the bit rate (Supplementary Section 2 shows the derivation).

At low temperatures, the resistance of the electromagnet drops and can be made to vanish if the normal metal is replaced with a superconductor. As a result, the energy per bit depends only on the modulation current and the inductance of the device. For our gold electrode, the resistance goes from 1.43 Ω at 300 K down to ~350 mΩ around 77 K, where it saturates. Although high-quality metals can have conductivities that are a hundred times larger at 4 K (that is, 100 times smaller resistance) compared with those at room temperature[32], evaporation-deposited gold suffers from grain boundaries formed during the deposition process, limiting the minimum achievable resistance (Supplementary Section 3.1). On the other hand, the inductance does not notably change with temperature and equals 0.3 nH for a 70-μm-diameter coil. The average energy per bit for the device is computed as a function of the modulation current amplitude ($T = 300$, 77 and 4 K with $r_b = 2$ Gbps; Fig. 2f). In the same figure, we also show the expected energy per bit when gold is replaced by a superconductor.

A relevant metric for an optical link is the optical modulation amplitude, which is defined as the difference between the high- and low-power levels in a bi-level optical signalling scheme[33]. When the input laser wavelength is parked at the −3 dB point of the modulator response curve (Fig. 2d), the high-power level does not notably change with respect to the resonance shift. As such, the ER can serve as a proxy metric for the optical modulation amplitude. Combining the calculated values of ER (Fig. 2e) with the energy per bit (Fig. 2f), we find that the largest ER can be achieved in a critically coupled ring ($\gamma = K = 0.063$) with an energy per bit of 2 pJ per bit ($r_b = 2$ Gbps; Fig. 2g). We can further reduce the energy

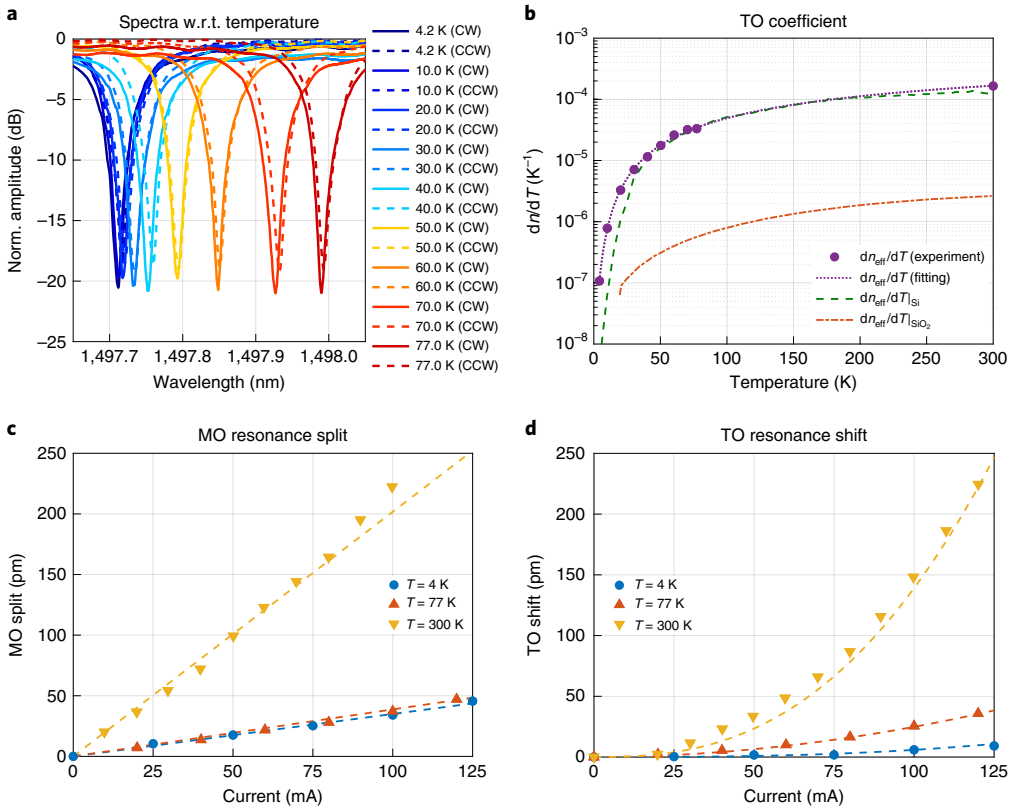

Fig. 3 | Characterization of TO and MO responses of the modulator at cryogenic temperatures. a, TO shift of the spectral response of the microring between 4 and 77 K when no current is injected in the electromagnet. The spectra for both CW (solid lines) and CCW (dashed lines) propagation spectra are shown. **b**, TO coefficient of the device extracted from the thermal shift of the spectra. For reference, the TO contribution of silica and silicon are also shown. **c**, MO split of the microring resonance when a current is injected in the electromagnet. The split between CW and CCW resonances ($2\times\Delta\lambda_{MO}$) increases linearly as a function of current magnitude at all temperatures. **d**, TO shift of the microring resonance when a current is injected in the electromagnet because of local Joule heating. As a guide for the eye, the experimental results have been fitted with a sub-quadratic curve (~I^b where $b<2$).

consumption by accepting a smaller ER. As such, ER as high as 10 dB can be achieved with less than 1 pJ per bit in an undercoupled ring ($\gamma=0.063$, $K=0.58\gamma=0.036$). In the same graph, we also report the energy per bit and ER for the device under test (DUT), which operates in the overcoupled regime ($\gamma=0.063$, $K=1.71\gamma=0.11$), yielding ER = 10 dB and $E_b=4$ pJ per bit.

The MO modulator is fabricated using a standard silicon photonic process. The silicon microring resonator and waveguide are patterned on a silicon-on-insulator (SOI) wafer with 220 nm silicon on top of 2 µm buried silicon dioxide (SiO_2). The Ce:YIG layer is grown on a separate SGGG substrate in a process that yields high-quality crystals. Subsequently, Ce:YIG is bonded to the silicon wafer in a flip-chip process based on plasma-activated SiO_2–SiO_2 covalent bonding at low temperatures[34]. After bonding, the SGGG is mechanically polished to reduce the distance between the electromagnet and deposited on top of the silicon/Ce:YIG interface (Methods provides more details on device fabrication). Using a straight silicon waveguide without Ce:YIG as a reference and evaluating the FWHM of the microring resonances, we estimate the interface loss due to the bonded layer to be about 0.6 dB per facet, whereas the propagation loss in the silicon/Ce:YIG waveguide is 13 dB cm^{-1} at 1,550 nm (Supplementary Section 3.2).

Device performance at cryogenic temperatures

The performance of the device was tested at cryogenic temperatures in a closed-cycle cryostat (Montana Cryostation s200) at temperatures ranging between 4 and 77 K. The TO resonance shift is determined from measurements of the microring spectral response when no current is applied to the electromagnet. By tracking the shift of the resonance with respect to temperature for both CW and CCW resonant modes (Fig. 3a), we extract the TO coefficient (Supplementary Section 3.4) as follows:

$$\frac{\mathrm{d}n_{\mathrm{eff}}}{\mathrm{d}T}=\frac{n_{\mathrm{g}}}{\lambda}\frac{\mathrm{d}\lambda}{\mathrm{d}T}. \tag{3}$$

This is plotted in Fig. 3b together with the computed TO contributions from silicon[5] and silica[28] for reference. At 4 K, a temperature increment of $\Delta T=1$ K causes the resonance to shift by less than 0.05 pm, making the TO effect negligible for our application. At higher temperatures, the TO shift increases, reaching 16.8 pm K^{-1} at 77 K and 80.0 pm K^{-1} at 300 K. In the temperature range from 4 to 77 K, we observe that the resonances in the two directions are not perfectly aligned, but their offset is a mere 3.7 ± 1.9 pm. This suggests the presence of a small residual in-plane magnetization in Ce:YIG (Supplementary Section 3.4).

When a current is injected in the electromagnet, Ce:YIG is locally magnetized and the optical response is no longer reciprocal. That is, the effective indices for the CW and CCW propagation directions are different, resulting in a splitting of the resonant wavelength for the two directions ('MO split'). As shown in Fig. 3c, the MO split changes linearly with the current amplitude and its value at 4 and 77 K is about five times lower than the corresponding value measured at 300 K for the same current (that is, the same magnetic field). As reported in Supplementary Section 3.4, Ce:YIG becomes magnetically harder at lower temperatures and a 110 mA

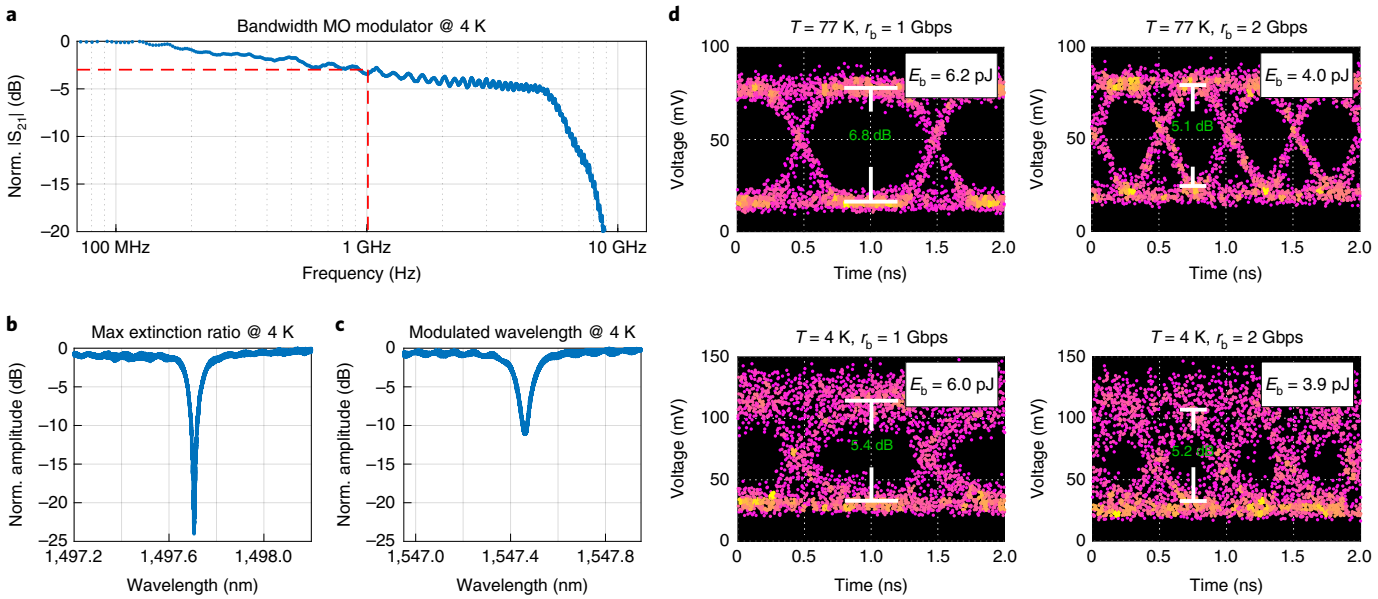

Fig. 4 | High-speed characterization of MO modulator at cryogenic temperatures. a, Frequency response (S_{21} coefficient) of the MO modulator at 4 K measured with a vector network analyser (VNA). The red dashed line highlights the point where S_{21} has decreased by 3 dB relative to the low-frequency value. The roll-off in this regime is 3 dB per decade, which is much less than the 20 dB per decade expected for a single-pole filter function. A sharper roll-off sets in at a frequency of 5 GHz. **b**,**c**, Spectral response of the microring resonator near 1,500 nm (**b**) and 1,550 nm (**c**). Although the spectrum near 1,500 nm shows sharper resonance, the characterization is performed near 1,550 nm because this wavelength is better suited for the testing apparatus. **d**, Eye diagram at bit rates of 1 Gbps (first column) and 2 Gbps (second column) measured at temperatures of 77 K (first row) and 4 K (second row). The eye diagram at 4 K shows a smaller ER compared with 77 K, which is mainly due to the difficulties in finely controlling the fibre-to-chip alignment at this temperature (Supplementary Section 3 provides more details on the measurement setup). In the inset, we report the energy consumption per bit computed from the independent measurements of R and L. The value of energy per bit, E_b, does not substantially change between 77 and 4 K because the ohmic dissipation in the electromagnet is the dominating contribution of the energy consumption and the resistance saturates below ~100 K (Supplementary Section 3).

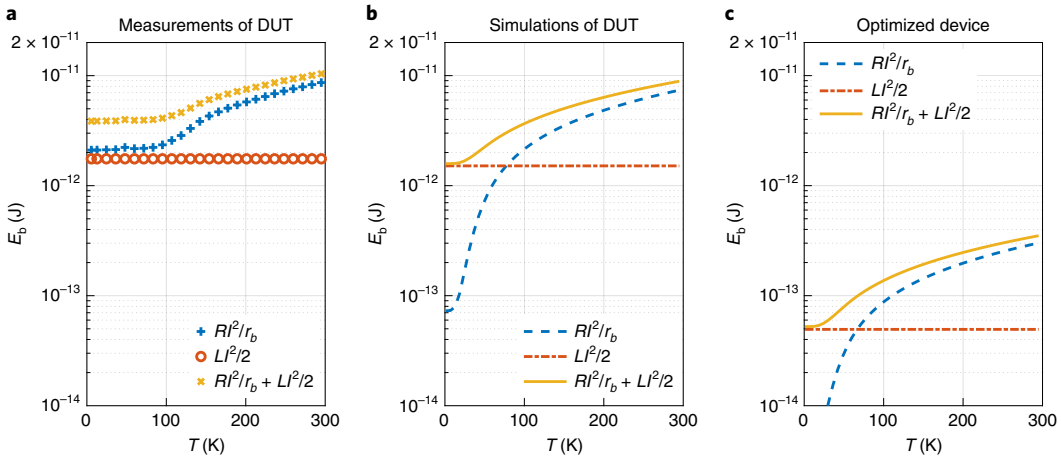

Fig. 5 | Energy per bit of the MO modulator as a function of temperature for a bit rate of 2 Gbps. a, Measured energy per bit of the DUT. The measured value of E_b is as low as 3.9 pJ per bit at 4 K and is limited by the resistance of the electromagnet. **b**, Simulated energy per bit of the DUT. A comparison between the simulations and measurements shows strong agreement for the inductive energy term, $LI^2/2$. However, the theoretical value of ohmic dissipation in the electromagnet, RI^2/r_b, shows room for improvement by reducing the cryogenic resistance of the electromagnet. **c**, Energy per bit that is achievable after optimizing the device by reducing the footprint, thinning the SGGG substrate and considering undercoupled resonators.

electrical current (1.5 mT magnetic field) is not sufficient to magnetically saturate it. Although the Faraday rotation of Ce:YIG is expected to increase for decreasing temperatures[17,26], a higher magnetic field is needed to reach such a value because of the stronger coercive force that limits the MO split at 77 and 4 K compared with the room-temperature case.

At very low temperatures, the resonance-wavelength shift is almost exclusively due to the MO effect. As shown in Fig. 3d, the TO shift drops substantially at 77 K and becomes negligible at 4 K. This is due to the enhanced conductivity of gold at cryogenic temperatures, leading to lower Joule heating, along with the previously discussed reduction in TO coefficient with decreasing temperatures.

We evaluate the performance of the modulator at cryogenic temperatures by measuring its bandwidth and its modulation fidelity when driven with high-speed data. For the first measurement, we use a tunable laser to generate an optical carrier at a wavelength near 1,550 nm, which couples in and out of the device via lensed fibres and is collected after modulation by a high-speed photodetector at room temperature. The radio-frequency input signal is generated by a vector network analyser and swept from 100 MHz to 20 GHz (Supplementary Section 3.5 provides more details on the experimental setup). The measured frequency response of the MO modulator is plotted in Fig. 4a, showing a reduction in modulation by 3 dB at around 1 GHz compared with the direct-current (d.c.) case at a temperature of 4 K. However, the roll-off is a mere 3 dB per decade in this regime, with a steeper roll-off setting in at around 5 GHz. The ultimate modulation bandwidth is limited by the magnetic response time of Ce:YIG, which is on the order of hundreds of picoseconds[14].

To further characterize the bandwidth of the device, we performed data modulation measurements by sending a pseudo-random non-return-to-zero bit sequence of length 2^9-1 to the modulator with a peak amplitude of 110 mA. To achieve a better signal-to-noise ratio, the modulated optical output signal is amplified by an erbium-doped fibre amplifier and filtered before reaching the photodetector, which is connected to a digital oscilloscope. For this measurement, the carrier wavelength is set close to 1,550 nm. Although the ER at around 1,550 nm is low compared with shorter wavelengths (Fig. 4b,c) and the resonator is slightly overcoupled at 1,550 nm ($K=0.11$ and $\gamma=0.063$), this wavelength offers the benefit of a high optical gain in the erbium-doped fibre amplifier. The recorded modulation eye diagrams for data rates of 1 and 2 Gbps are shown in Fig. 4d at both 77 and 4 K. Recalling the results shown in Fig. 3c, we need five times higher current at these temperatures than at room temperature to achieve the same MO split. On the other hand, the smaller MO split in Ce:YIG is compensated by the lower electrical resistivity in metals at cryogenic temperatures, which means that the power consumption of the modulator is less penalized by the large drive current.

The potential for high energy efficiency in a low-impedance system is one of the major benefits of the cryogenic MO modulator. As shown in Fig. 4d, we experimentally measured an eye diagram up to 2 Gbps with an energy consumption as low as 3.9 pJ per bit at 4 K. The transduction gain (number of optical photons transduced per microwave photon on the input[2]) is ~10^{-8} when measured in a 50 Ω system. A similar value was measured in lithium niobate electro-optic modulator[2], but in the MO case, the transduction gain is inversely proportional to the impedance of the system (Supplementary Section 4), making it ideal for superconducting circuits.

Achieving superior performance

We project that the performance of the device can be vastly improved with straightforward optimizations of the modulator design and fabrication. In the DUT, the value of energy per bit is limited by the resistance of the electromagnet (Fig. 5a). Ohmic dissipation can be reduced by improving the quality of the electromagnet or replacing it with a superconducting magnet, leading to $E_b \approx LI^2/2 = 1.5$ pJ per bit at 4 K (Fig. 5b). From this point, the energy per bit can be further lowered by reducing the inductance of the electromagnet and decreasing the modulation current. In the tested device, the measured value of L is 0.3 nH, which can be reduced to 0.2 nH by considering a microring with a diameter of 40 µm (Supplementary Section 3.1). The current required for modulation can be reduced in two ways: by considering an undercoupled resonator with the same ER, which yields a reduction in current of 50% (Fig. 2e); and by decreasing the distance between the electromagnet and silicon/Ce:YIG interface from 5.5 µm to 1.5 µm, which can be done by replacing the mechanical polishing of the SGGG with a selective etching process, resulting in a reduction in the required current amplitude by up to another factor of 2.25 (Supplementary Section 5). With these feasible design improvements, the energy per bit of the device can be reduced by more than 30 times (Fig. 5c), thus achieving an energy consumption as low as 50 fJ per bit.

Superior performance is expected by replacing YIG with novel MO materials under development. At 4 K, europium sulfide (EuS) and europium selenide (EuSe) have a Faraday rotation constant that is 150 and 300 times larger than that of YIG (ref. [16]), respectively, allowing for a reduction in modulation current to a few tens of microamperes. The use of those materials will also benefit the transduction gain, increasing its value by five orders of magnitude. The time response of YIG is limited by its ferromagnetic resonance[14], but a much faster response can be accomplished with terbium-doped EuS or cadmium manganese telluride ($Cd_{1-x}Mn_xTe$) that can support a modulation rate of tens of gigahertz[35,36].

Conclusions

Although the DUT was tested in a 50 Ω environment, the most important application of the modulator is as an interface to low-impedance logic based on Josephson junctions. Such logic has the potential to perform classical computations at a fraction of the energy cost of room-temperature complementary metal–oxide–semiconductor technology[37–39]. Its use for the control and readout of superconducting qubits has also been identified to be a promising path towards the scaling of such quantum processors[1–3]. To achieve sufficient output currents to drive the MO modulator, all-superconducting driving elements can be used, similar to those that have been developed to interface superconducting logic with magnetic memory[40]. Because of their integration with superconducting circuitry, our MO modulators have the potential to enable efficient data transfer in large-scale classical and quantum information systems.

Methods

Device fabrication. A 220 nm SOI wafer with 2 µm buried oxide was patterned using a 248 nm ASML 5500 deep-ultraviolet stepper, and dry etched using a Bosch process (Plasma-Therm 770) to form the waveguides and resonators. For wafer bonding, both SOI and Ce:YIG/SGGG samples are rigorously cleaned, and activated with O_2 plasma (EVG 810). Ce:YIG is directly bonded onto the SOI patterns using a flip-chip bonder (Finetech) and then annealed at 200 °C for 6 h under 3 MPa pressure to strengthen the bond. The required alignment accuracy is fairly tolerant (~200 µm). After bonding, a 1 µm layer of SiO_2 is sputtered everywhere on the chip as an upper cladding. Next, the SGGG substrate is thinned by mounting the sample against a flat chuck and polishing (Allied Technologies) using a series of increasingly fine lapping films. The thickness of SGGG is monitored using a micrometer and confirmed to be ~5 µm with a separate Dektak profilometry measurement. Variation of thickness across the sample is roughly ±1.5 µm due to imperfect levelling of the chuck. The patterns for metal coils and contacts are defined on the backside of the SGGG with a 365 nm GCA i-line wafer stepper. Then, 22 nm Ti is deposited as an underlayer, followed by 1.5 µm Au using electron-beam evaporation, and the metal coils and contacts are released with a lift-off procedure. Finally, the sample is diced and the facets are polished.

Data availability

The data that support the findings of this study are available from the corresponding author upon reasonable request.

Code availability

The computer code used in this study is available from the corresponding author upon reasonable request.

Received: 18 June 2021; Accepted: 25 July 2022;
Published online: 5 September 2022

References

1. Lecocq, F. et al. Control and readout of a superconducting qubit using a photonic link. *Nature* **591**, 575–579 (2021).
2. Youssefi, A. et al. A cryogenic electro-optic interconnect for superconducting devices. *Nat. Electron.* **4**, 326–332 (2021).
3. Reilly, D. J. Challenges in scaling-up the control interface of a quantum computer. In *2019 IEEE International Electron Devices Meeting (IEDM)* 31.7.1–31.7.6 (IEEE, 2019).

4. Silverstone, J. W., Bonneau, D., O'Brien, J. L. & Thompson, M. G. Silicon quantum photonics. *IEEE J. Sel. Topics Quantum Electron.* **22**, 390–402 (2016).
5. Komma, J., Schwarz, C., Hofmann, G., Heinert, D. & Nawrodt, R. Thermo-optic coefficient of silicon at 1550 nm and cryogenic temperatures. *Appl. Phys. Lett.* **101**, 041905 (2012).
6. Sze, S. M. & Ng, K. K. *Physics of Semiconductor Devices* (John Wiley & Sons, 2006).
7. Gehl, M. et al. Operation of high-speed silicon photonic micro-disk modulators at cryogenic temperatures. *Optica* **4**, 374–382 (2017).
8. Pintus, P. et al. Characterization of heterogeneous InP-on-Si optical modulators operating between 77 K and room temperature. *APL Photonics* **4**, 100805 (2019).
9. Eltes, F. et al. An integrated optical modulator operating at cryogenic temperatures. *Nat. Mater.* **19**, 1164–1168 (2020).
10. Chakraborty, U. et al. Cryogenic operation of silicon photonic modulators based on d.c. Kerr effect. *Optica* **7**, 1385–1390 (2020).
11. Lee, B. S. et al. High performance integrated graphene electro-optic modulator at cryogenic temperature. *Nanophotonics* **10**, 99–104 (2021).
12. Dötsch, H. et al. Applications of magneto-optical waveguides in integrated optics: review. *J. Opt. Soc. Am. B* **22**, 240–253 (2005).
13. Stadler, B. J. H. & Mizumoto, T. Integrated magneto-optical materials and isolators: a review. *IEEE Photon. J.* **6**, 1–15 (2014).
14. Chau, K. J., Irvine, S. E. & Elezzabi, A. Y. A gigahertz surface magneto-plasmon optical modulator. *IEEE J. Quantum Electron.* **40**, 571–579 (2004).
15. Firby, C. J. & Elezzabi, A. Y. High-speed nonreciprocal magnetoplasmonic waveguide phase shifter. *Optica* **2**, 598–606 (2015).
16. Sobolewski, R. & Park, J. R. Magneto-optical modulator for superconducting digital output interface. *IEEE Trans. Appl. Supercond.* **11**, 727–730 (2001).
17. Lage, E. et al. Temperature-dependent Faraday rotation and magnetization reorientation in cerium-substituted yttrium iron garnet thin films. *APL Mater.* **5**, 036104 (2017).
18. Likharev, KonstantinK. & V., K. S. RSFQ logic/memory family: a new Josephson-junction technology for sub-terahertz-clock-frequency digital systems. *IEEE Trans. Appl. Supercond.* **1**, 3–28 (1991).
19. Mukhanov, O. A. Energy-efficient single flux quantum technology. *IEEE Trans. Appl. Supercond.* **21**, 760–769 (2011).
20. Fedorov, K. G., Shcherbakova, A. V., Wolf, M. J., Beckmann, D. & Ustinov, A. V. Fluxon readout of a superconducting qubit. *Phys. Rev. Lett.* **112**, 160502 (2014).
21. Opremcak, A. et al. Measurement of a superconducting qubit with a microwave photon counter. *Science* **361**, 1239–1242 (2018).
22. Howington, C. et al. Interfacing superconducting qubits with cryogenic logic: readout. *IEEE Trans. Appl. Supercond.* **29**, 1–5 (2019).
23. OIDA. OIDA quantum photonics roadmap: every photon counts. *OIDA Rep.* **3** (2020).
24. Gabriel, G. J. & Brodwin, M. E. The solution of guided waves in inhomogeneous anisotropic media by perturbation and variational methods. *IEEE Trans. Microw. Theory Tech.* **13**, 364–370 (1965).
25. Bogaerts, W. et al. Silicon microring resonators. *Laser Photon. Rev.* **6**, 47–73 (2012).
26. Ostoréro, J., Escorne, M., Gouzerh, J. & Le Gall, H. Magnetooptical properties of Ce-doped YIG single crystals. *J. Phys. IV France* **07**, C1-719–C1-720 (1997).
27. Pintus, P., Tien, M. C. & Bowers, J. E. Design of magneto-optical ring isolator on SOI based on the finite-element method. *IEEE Photon. Technol. Lett.* **23**, 1670–1672 (2011).
28. Elshaari, A. W., Zadeh, I. E., Jöns, K. D. & Zwiller, V. Thermo-optic characterization of silicon nitride resonators for cryogenic photonic circuits. *IEEE Photon. J.* **8**, 2701009 (2016).
29. Sacher, W. D. & Poon, J. K. S. Dynamics of microring resonator modulators. *Opt. Express* **16**, 15741–15753 (2008).
30. Li, G. et al. Ring resonator modulators in silicon for interchip photonic links. *IEEE J. Sel. Topics Quantum Electron.* **19**, 3401819 (2013).
31. Dube-Demers, R. et al. Analytical modeling of silicon microring and microdisk modulators with electrical and optical dynamics. *J. Light. Technol.* **33**, 4240–4252 (2015).
32. Haynes, W. M., Lide, D. R. & Bruno, T. J. *CRC Handbook of Chemistry and Physics (2016–2017)* (CRC Press, 2016).
33. Maxim Integrated Products. Optical modulation amplitude (OMA) and extinction ratio. *Appl. Note HFAN-02.2.2* 1–5 (2008).
34. Liang, D. et al. Low-temperature, strong SiO_2-SiO_2 covalent wafer bonding for III–V compound semiconductors-to-silicon photonic integrated circuits. *J. Electron. Mater.* **37**, 1552–1559 (2008).
35. Freeman, M. R. Picosecond pulsed-field probes of magnetic systems (invited). *J. Appl. Phys.* **75**, 6194–6198 (1994).
36. Rey-De-Castro, R. et al. Subpicosecond Faraday effect in $Cd_{1-x}Mn_xTe$ and its application in magneto-optical sampling. *Appl. Phys. Lett.* **85**, 3806–3808 (2004).
37. Holmes, D. S., Ripple, A. L. & Manheimer, M. A. Energy-efficient superconducting computing—power budgets and requirements. *IEEE Trans. Appl. Supercond.* **23**, 1701610–1701610 (2013).
38. Holmes, D. S., Kadin, A. M. & Johnson, M. W. Superconducting computing in large-scale hybrid systems. *IEEE Comput. Soc.* **48**, 34–42 (2015).
39. Tolpygo, S. K. Superconductor digital electronics: scalability and energy efficiency issues. *Low Temp. Phys.* **42**, 361–379 (2016).
40. Nguyen, M. H. et al. Cryogenic memory architecture integrating spin Hall effect based magnetic memory and superconductive cryotron devices. *Sci. Rep.* **10**, 248 (2020).

Acknowledgements

We would like thank G. E. W. Bauer, P. Morton and J. Peters for the useful discussions. P.P. and J.E.B. acknowledge support from the Air Force Office of Scientific Research under award no. FA9550-21-1-0042. P.P., L.R., M.V.G., M.S. and J.E.B. acknowledge support from the Army Research Office under contract no. W911NF-19-C-0060. Any opinions, findings, and conclusions or recommendations expressed in this material are those of the authors and do not necessarily reflect the views of the United States Air Force nor the Army Research Office. P.P. and J.E.B. also acknowledge Microsoft Research for supporting this research.

Author contributions

P.P. conceived and designed the device, performed the modelling and analysed the performance. P.P., L.R., S.P. and M.V.G. performed the d.c. and radio-frequency measurements at cryogenic temperatures. D.H. performed the mask layout and fabricated the device. P.P. and G.A.C. performed the radio-frequency simulations. P.P., L.R., S.P. and F.K. performed the analysis of energy consumption. Y.S., Y.T. and T.M. grew the Ce:YIG samples and provided the MO material characterization. P.P., M.S. and J.E.B. supervised and coordinated the project. All the authors contributed to the preparation of the manuscript.

Competing interests

P.P. and J.E.B. filed the US provisional patent application no. 63/224,487 for an MO modulator. The remaining authors declare no competing interests.

Additional information

Supplementary information The online version contains supplementary material available at https://doi.org/10.1038/s41928-022-00823-w.

Correspondence and requests for materials should be addressed to Paolo Pintus.

Peer review information *Nature Electronics* thanks Jeremy Witzens and the other, anonymous, reviewer(s) for their contribution to the peer review of this work.

Reprints and permissions information is available at www.nature.com/reprints.

Publisher's note Springer Nature remains neutral with regard to jurisdictional claims in published maps and institutional affiliations.